

# Recycled Photons Traveling Several Millimeters in Waveguides Based on CsPbBr<sub>3</sub> Perovskite Nanocrystals

Juan Navarro-Arenas, Isaac Suárez,\* Andrés F. Gualdrón-Reyes, Iván Mora-Seró, Juan Bisquert, and Juan P. Martínez-Pastor\*

Reabsorption and reemission of photons, or photon recycling (PR) effect, represents an outstanding mechanism to enhance the carrier and photon densities in semiconductor thin films. This work demonstrates the propagation of recycled photons over several mm by integrating a thin film of CsPbBr<sub>3</sub> nanocrystals into a planar waveguide. An experimental set-up based on a frequency modulation spectroscopy allows to characterize the PR effect and the determination of the effective decay time of outcoupled photons. A correlation between the observed photoluminescence redshift and the increase of the effective decay time is demonstrated, which grows from 3.5 to near 9 ns in the best device. A stochastic Monte Carlo model reproduces these experimental results and allows the extraction of the physical mechanisms involved. In the waveguide under study recycled photons follow a drift (directional enhancement) velocity  $\approx 5.7 \times 10^5 \text{ m s}^{-1}$ , dominating over the diffusive regime observed in a standard thin film ( $D \approx 420 \text{ m}^2 \text{ s}^{-1}$ ). This means that recycled photons propagate mm-distances in shorter traveling times in the waveguide ( $\approx 5 \text{ ns}$ ) as compared to the film ( $>20 \text{ ns}$ ). These results are expected to pave the road for exploiting the PR effect in future optoelectronic and photonic devices.

Such multiple (re)absorption/(re)emission cycles result in a certain population of “recycled photons” concentrated inside the semiconductor. Consequently, an efficient PR effect provides another degree of freedom to control the photon and carrier densities in a semiconductor<sup>[2]</sup> and hence a way to tailor-made its optoelectronic properties.<sup>[3,4]</sup> Demonstrated applications include solar cells, light-emitting diodes, or optical modulators.<sup>[2]</sup> In this context, PR has been recently claimed in halide perovskites (HP), as an effect that could contribute to a certain extent to the excellent conversion efficiencies and emission rates reported for this family of semiconductors.<sup>[5,6]</sup> Indeed, the strong absorption coefficient above the bandgap and sharp (excitonic) band edge,<sup>[7,8]</sup> the small Stokes shift (SS) between photoluminescence (PL) and absorption,<sup>[9,10]</sup> and the high PL quantum yield (PLQY)<sup>[11,12]</sup> are outstanding characteristics of HPs and needed ingredients

for leading to important PR effect. In this way, over the last 3–4 years, different experimental and theoretical reports have analyzed the efficiency of PR in HPs and the potential benefits in solar cells<sup>[13–15]</sup> or light-emitting diodes,<sup>[15,16]</sup> among other devices.<sup>[15]</sup> In particular, experimental studies carried out in CH<sub>3</sub>NH<sub>3</sub>PbX<sub>3</sub> (X = Cl, Br, I) polycrystalline thin films,<sup>[17,18]</sup> CH<sub>3</sub>NH<sub>3</sub>PbX<sub>3</sub> single crystals,<sup>[10,19,20]</sup> CsPbBr<sub>3</sub> nano/microwires<sup>[21–23]</sup> or CsPbBr<sub>3</sub> nanocrystals<sup>[9]</sup> always show that PL spectra experience an important redshift and an elongation of the decay time after traversing some microns of the HP material. Although there has been a controversy about the impact of PR in the total PL spectra,<sup>[19,24]</sup> or if PR dominates or not over carrier diffusion on the effective decay time,<sup>[23,25]</sup> recent studies on perovskite single crystals<sup>[6]</sup> and MAPI polycrystalline thin films<sup>[18]</sup> confirm that PR is the dominant transport mechanism for propagation lengths longer than the diffusion of carriers. Besides, the theoretical analysis predicts that multiple absorption and emission processes produce a certain “diffusive regime of traveling photons” that increases the effective lifetime of photons outcoupled from the sample (thin film, microwire, single crystal ...).<sup>[26]</sup>

Indeed, recent theoretical and experimental works demonstrated an enhancement of the open-circuit voltage in solar cells<sup>[14,18,27,28]</sup> or radiation efficiency in light-emitting diodes<sup>[29]</sup> when PR is optimized. The standard optical configuration that has been chosen to demonstrate the PR effect in most works consists of a semiconductor thin film deposited on a specific


## 1. Introduction

Photon recycling (PR) is a physical mechanism from which a fraction of the photons radiatively generated by a semiconductor is sequentially absorbed and emitted before being extracted.<sup>[1]</sup>

Dr. J. Navarro-Arenas, Prof. J. P. Martínez-Pastor  
Instituto de Ciencia de Materiales (ICMUV)  
Universidad de Valencia  
C/ Catedrático José Beltrán, 2, Paterna 46980, Spain  
E-mail: juan.mtnez.pastor@uv.es

Dr. I. Suárez  
Escuela Técnica Superior de Ingeniería  
Universidad de Valencia  
C/Avenida de la Universidad s/n, Burjassot 46100, Spain  
E-mail: isaac.suarez@uv.es

Dr. A. F. Gualdrón-Reyes, Prof. I. Mora-Seró, Prof. J. Bisquert  
Institute of Advanced Materials (INAM)  
University Jaume I  
Avenida de Vicent Sos Baynat s/n, Castellón 12071, Spain

 The ORCID identification number(s) for the author(s) of this article can be found under <https://doi.org/10.1002/adom.202100807>.

© 2021 The Authors. Advanced Optical Materials published by Wiley-VCH GmbH. This is an open access article under the terms of the Creative Commons Attribution-NonCommercial License, which permits use, distribution and reproduction in any medium, provided the original work is properly cited and is not used for commercial purposes.

DOI: 10.1002/adom.202100807

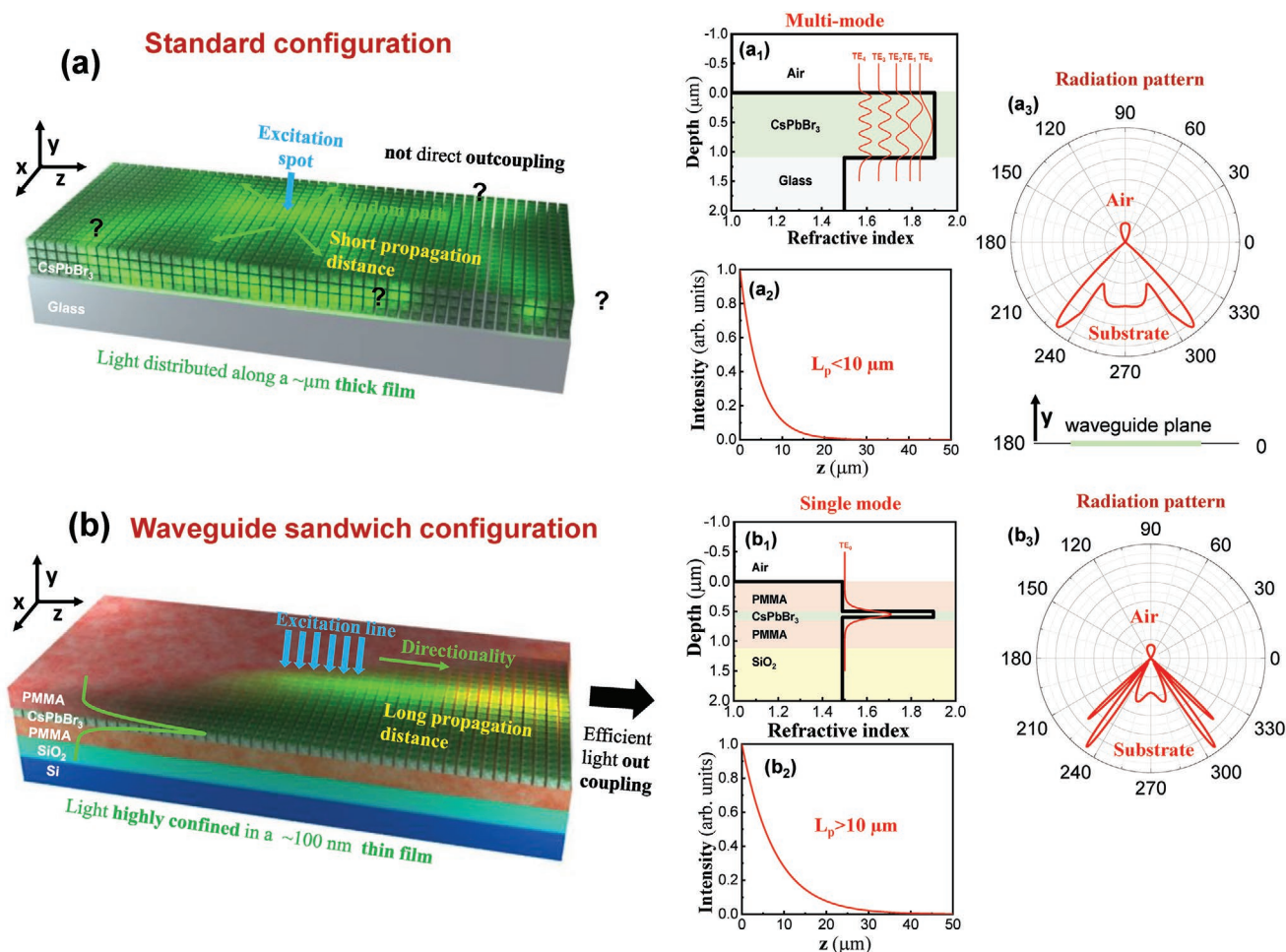


**Figure 1.** Difference between the standard and the sandwich waveguide configurations. a) The standard configuration consists of a thick PNC layer deposited on the substrate where the emitted photons are randomly distributed in the active film. a<sub>1</sub>) This film behaves as a multimode waveguide. a<sub>2</sub>) Propagation of the light follows the law  $e^{-\alpha z}$  with  $\alpha > 0.2 \mu\text{m}^{-1}$  due to the self-absorption and scattering losses. a<sub>3</sub>) Radiation pattern indicates the emission not guided by the film. b) The waveguide structure proposed in this work consists of a thin PNC layer sandwiched between two PMMA claddings. b<sub>1</sub>) The index contrast between the different materials results in the single-mode propagation of the  $\text{TE}_0$  ( $\text{TM}_0$ ) highly confined in the active film. b<sub>2</sub>) PMMA claddings alleviate the attenuation. b<sub>3</sub>) The radiation pattern indicates that the claddings recover some radiated light.

substrate, see **Figure 1a**.<sup>[13,16,18,19,30]</sup> Nevertheless, the random propagation of the photons in this simple architecture does not favor long propagation distances nor confinement of light, and hence it does not provide an efficient extraction/use of the recycled photons. In fact, the design of the optical architecture can significantly increase the PR efficiency. In this sense, more sophisticated examples found in literature include the use of HP nanofilms/microwires where emitted photons can propagate over tenths of microns,<sup>[18]</sup> scattering with silver nanoparticles to increase the effective length of the optical path for emitted photons,<sup>[31]</sup> or the enhancement of outcoupled light (low-index/high-index layer structure, textured substrate, and active layer).<sup>[32,33]</sup> These configurations, however, are again limited by the absence of a directional path for the emitted photons, the lack of an efficient mechanism to extract the light, or nonradiative plasmonic losses if metal nanoparticles are integrated. The ideal photonic structure should confine the PL in the HP, enable a long path for emitted photons, and provide an efficient light outcoupling at a desired place of the HP active layer.

In this work, we propose a photonic architecture that fulfills all necessary conditions to optimize PR on HP films. This structure consists of a thin (50–200 nm) semiconductor layer sandwiched between two poly(methyl methacrylate) (PMMA) films, see **Figure 1b**. This elegant planar waveguide configuration efficiently exploits the efficient emission properties of the semiconductor by the high confinement of light within the active layer, provides an in-plane light propagation with a reduced attenuation due to the absence of losses in the polymer, and allows efficient extraction of emitted light (waveguided PL) by end-fire coupling or diffraction grating methods. Indeed, we have already used this configuration for the case of CdSe/ZnS quantum dots (QD)<sup>[34]</sup> or organic compounds<sup>[35]</sup> as active layers, in order to demonstrate an enhancement of the waveguided PL or an efficient optical amplification, respectively. Thin films based on CsPbBr<sub>3</sub> perovskite nanocrystals (PNCs) are chosen here as the active material with appropriate absorption and emission features given above. Layers of PNCs have demonstrated excellent performances for light emission,<sup>[36]</sup>

optical amplification,<sup>[37–39]</sup> and photovoltaics.<sup>[40]</sup> Despite these promising properties, the study of PR on perovskites has been mainly focused on CH<sub>3</sub>NH<sub>3</sub>PbI<sub>3</sub> (MAPI) films or single crystals, while the choice of PNCs was made in a few works.<sup>[9]</sup>

The proposed PMMA/PNC/PMMA waveguide architecture represents a suitable photonic structure for efficient propagation of recycled photons up to several millimeters, as we demonstrate in this work. In fact, the effective PR propagation length is obtained experimentally in the mm range, which is near two orders of magnitude longer than estimations in perovskite single crystals,<sup>[6,41]</sup> microwires,<sup>[21]</sup> or polycrystalline thin films.<sup>[18]</sup> We have measured an increased effective decay time for outcoupled photons increasing with the length of the waveguide, from 3.5 ns to about 9 ns. A combination of the variable stripe length method<sup>[42]</sup> with a frequency modulated PL technique<sup>[43]</sup> is used in the present work in a similar way to the case of the study of carrier transport. This set-up analyzes the dependence of the emitted PL as a function of a modulating frequency (40 kHz to 2 MHz in our case) of the excitation laser, as recently proposed by Ansari-Rad and Bisquet,<sup>[44]</sup> in order to extract the recombination parameters (traps, diffusion, non-radiative channels ...) at time scales ranging between 1 ns and several  $\mu$ s. To explain these results, we have first quantified the effect of PR as a feedback mechanism for carriers introduced in a rate equation model indicating that the PR effect could be interpreted as gain, but leading to compensation of losses during propagation. However, although a set of rate equations are usually chosen to theoretically predict the consequences of the PR effect,<sup>[6,18,23–26]</sup> they cannot easily incorporate the evolution of the photons with the propagation distance and the effect of the reabsorption in the shape of the PL spectrum. For this reason, we proposed a stochastic Monte Carlo model that reproduces both such experimental PL redshift and delay time introduced by photon reabsorption/reemission events during propagation in the PR effect. The model predicts more than 30 recycled photon events per injected/pumping photon and mm-propagation, which is possible by the relatively high PL quantum yield (relatively small influence of nonradiative recombination). The secondary photon flux formed by recycled photons in our optical waveguides can be interpreted as a Gaussian beam propagating with a dominating drift behavior with velocity  $5.7 \times 10^5$  m s<sup>-1</sup>, as compared to the diffusive character of PR in a standard thin film (without PMMA covers). Such “drift velocity” yields a “transit time” to travel 3 mm (until outcoupling) very close to the delay time deduced from experiment ( $\approx$ 5 ns). These results are conceptually new as compared to previous knowledge and the proposed architecture (producing light confinement) represents a suitable configuration to enhance the PR effect with potential applications in photovoltaics and light-emitting diodes, among other applications (fluorescent converters, for example).

## 2. A Suitable Architecture for Enhancing the Propagation of Recycled Photons

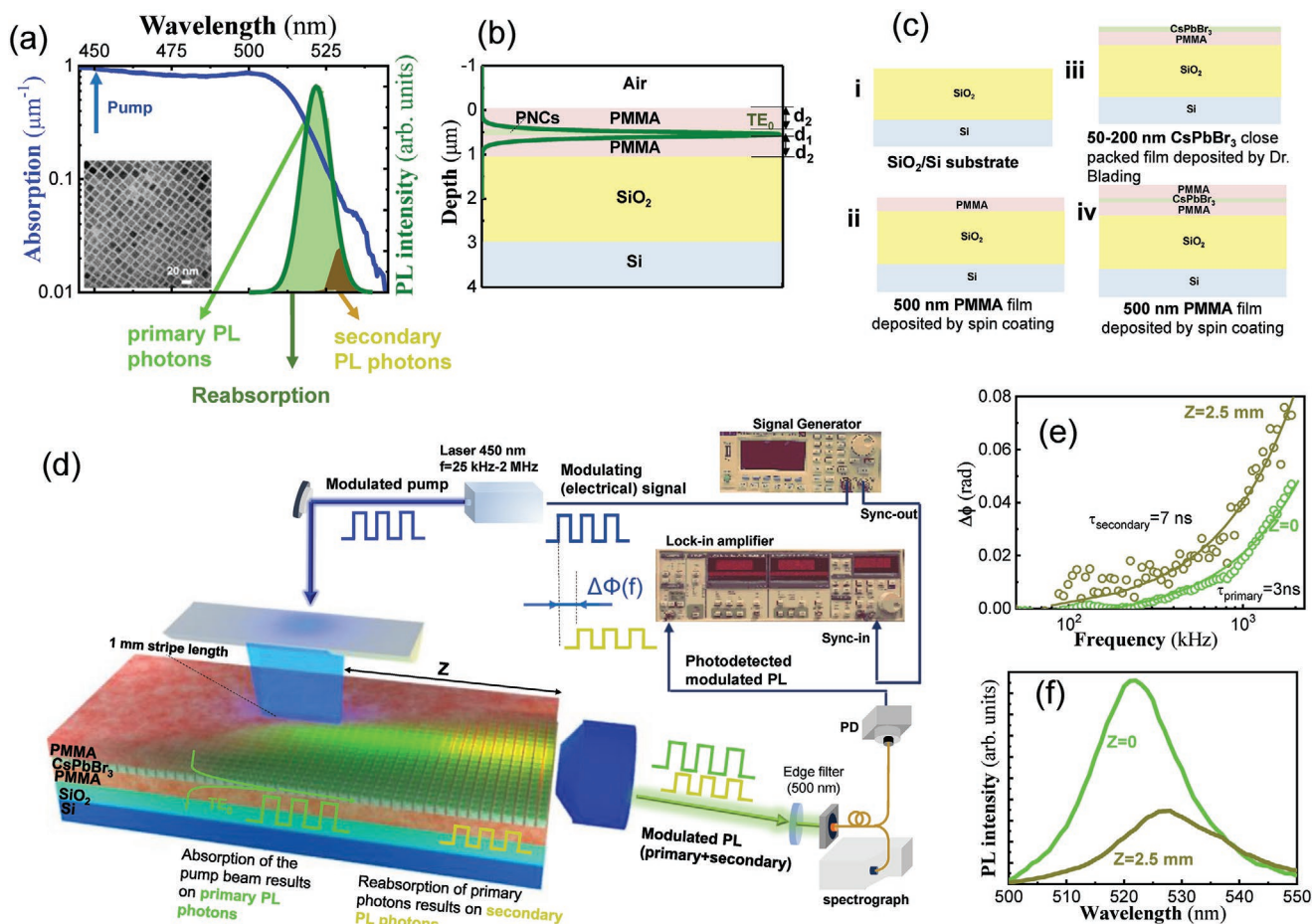
The common configuration chosen to analyze the PR consists of a  $\approx$  1  $\mu$ m thick film of the semiconductor deposited on a given substrate and illuminated by a small spot, see the

illustration in Figure 1a. Propagation of recycled photons in this structure takes place through optical modes depicted in Figure 1a<sub>1</sub>, and hence restricted to distances in the range of 10  $\mu$ m due to absorption and scattering losses (Figure 1a<sub>2</sub>), and some emitted light is lost through air or substrate radiative modes (Figure 1a<sub>3</sub>). Here, propagation modes and the respective effective refractive indices are obtained with a transfer matrix method algorithm,<sup>[45]</sup> losses ( $\alpha$ ) are estimated from the imaginary part of the effective refractive index at the operation wavelength ( $\alpha = 4 \cdot \pi \cdot \text{Im}(N_{\text{eff}})/\lambda$ ) and the radiation pattern is calculated considering dipole sources in the planar structures following the method detailed elsewhere.<sup>[46]</sup> Moreover, the illumination of this thin film by a small spot results in a random path for the emitted photons and, with it, in a limited PR effect and poor photon extraction/outcoupling efficiencies.

In the present work, this structure is replaced by the sandwich-like optical waveguide configuration illuminated by a stripe line, Figure 1b. This alternative geometry consists of a thin film (50–200 nm) of PNCs sandwiched between two PMMA layers and deposited onto a commercial SiO<sub>2</sub>/Si wafer (see Figure 1b and more details in Section S1 of the Supporting Information). In particular, this architecture is based on the different index contrast between the PNC layer ( $n = 1.9 - 0.009i$  at 520 nm),<sup>[47]</sup> the PMMA claddings ( $n = 1.492$  at 520 nm),<sup>[48]</sup> the air ( $n = 1$ ), and the SiO<sub>2</sub> ( $n = 1.4613$  at 520 nm) films.<sup>[48]</sup> Thicknesses of the layers are properly designed to provide the single-mode propagation of the TE<sub>0</sub> (TM<sub>0</sub>) mode highly confined within the active thin film, see Figure 1b<sub>1</sub>. Indeed, the mode size, defined as the depth where the maximum of the power distribution of the mode decreases to  $1/e^2$ , calculated for this mode is around  $0.57 \cdot \lambda$ , which is  $> 3$  times smaller than the modes propagated along a standard thin film  $\approx$ 1  $\mu$ m thick (Figure 1a). In this way, the emitted PL will be concentrated in a small volume (depth at  $1/e^2 \approx$  100 nm) which optimizes the light-matter interaction and reabsorption/reemission probability in the same way as a nanowire does in a polariton cavity.<sup>[49]</sup> Besides, the PMMA claddings alleviate the attenuation of propagating light, see Figure 1b<sub>2</sub>, and recover part of the radiated light, see Figure 1b<sub>3</sub>. Finally, the illumination by a stripe proposed here increases the production and provides a preferential direction for the propagation of emitted light, resulting in long traveling paths and the enhanced extraction of recycled photons by end-fire coupling techniques. Thus, in the proposed structure, the (re)absorption–(re)emission events are significantly enhanced and a large proportion of recycled photons can propagate along longer distances in shorter times as compared to the case of the standard film. Indeed, after a certain propagation distance, emitted photons propagating along the waveguide will come from a secondary photon flux (photons suffering several (re)absorption–(re)emission cycles), which will be efficiently outcoupled from the edge of the waveguide. In the last section of the manuscript, we will present theoretical simulations that demonstrate semiquantitatively these asseverations and hence the observed experimental results described below.

The CsPbBr<sub>3</sub> PNCs used in this work were grown following the hot-injection method developed by Kovalenko et al.<sup>[12]</sup> with some modifications detailed elsewhere.<sup>[39]</sup> Synthesized PNCs present a cubic shape (see inset in Figure 2a) with an average size ( $L$ ) of 9 nm and a size dispersion of 1.5 nm, approximately.





**Figure 2.** Analysis of the waveguide structure. a) Absorption (blue line and left axis) and PL (green line and right axis) measured in a 100 nm thick layer of CsPbBr<sub>3</sub> PNCs; the inset shows a low-resolution TEM image of the PNCs. b) Scheme of the sample: a CsPbBr<sub>3</sub> close-packed thin film ( $d_1 = 50\text{--}200$  nm) is sandwiched between two PMMA cladding layers ( $d_2 = 500$  nm); the green curve represents the power distribution of the TE<sub>0</sub> mode in a waveguide with  $d_1 = 100$  nm. c) Fabrication procedure. d) Experimental set-up used to measure frequency-modulated waveguided PL. e) Phase shift measured for  $z = 0$  (green) and  $z = 2.5$  mm (dark yellow). This shift is associated with a different decay time. f) PL spectra obtained at the output edge of the waveguide at  $z = 0$  (green) and  $z = 2.5$  mm (dark yellow).

The ratio  $L/2a_0$ , where  $a_0$  is the Bohr radius, is only 1.3, which corresponds to a weak quantum size confinement regime.

The absorption spectrum at room temperature of a thin film made of CsPbBr<sub>3</sub> PNCs exhibits an excitonic resonance at 509 nm (blue curve in Figure 2a) with a high absorption coefficient  $\approx 1 \mu\text{m}^{-1}$ , in agreement with results reported in previous publications for similar PNCs.<sup>[12,39]</sup> Similarly, the PL spectrum (green curve in Figure 2a) measured under back-scattering geometry in the same film at low excitation fluency ( $\approx 10 \text{ W cm}^{-2}$ ) shows a Gaussian shape centered at 520 nm with a full width at half maximum (FWHM) of 20 nm. The absorption coefficient at the PL peak wavelength, 522 nm, is  $\approx 0.1 \mu\text{m}^{-1}$ ,<sup>[39]</sup> which would result in a propagation length at this wavelength (at  $1/e$ ) inside a PNC film of around  $\approx 10 \mu\text{m}$ . The self-absorption phenomenon over sufficiently long optical paths  $\gg 10 \mu\text{m}$  has important consequences in the behavior of a photonic architecture containing PNCs. For example, it determines the observation of the amplified stimulated emission toward the red side of the excitonic spontaneous emission spectrum, effect that becomes more important in thicker films.<sup>[10,39]</sup>

Besides, since the PLQY reported for PNCs is above 40%<sup>[12]</sup> the reabsorption of the primary flux of photons initially emitted by the radiative exciton recombination in CsPbBr<sub>3</sub> PNCs would give rise to the creation of a secondary flux of photons at longer wavelengths (whose spectrum is illustrated by the brown shadowed curve in Figure 2a), due to the strong overlap between PL and absorption spectra below 525 nm, where the absorption coefficient increases from  $0.1$  to  $1 \mu\text{m}^{-1}$ . Consequently, the waveguided PL photons extracted at a certain distance would contain two different contributions: i) primary emitted photons not absorbed by the film along the propagation direction and ii) secondary photons generated from multiple (re)absorption and (re)emission processes.<sup>[5]</sup> The ratio between both contributions, (i)/(ii), will decrease with the propagation distance until outcoupling. A certain thickness dependence would also appear by the overlap between the waveguide propagation mode and the active material. In particular, the PMMA/PNC/PMMA sandwich-like waveguide geometry proposed in this work (Figure 2b) optimizes the absorption and generation of light compared to the case of the single thin film, as we

demonstrated for colloidal QDs<sup>[34]</sup> and organic compounds.<sup>[35]</sup> The steps followed to fabricate the sandwich-like waveguide are depicted in Figure 2c (see Section 1 of the Supporting Information for more details).

The experimental set-up chosen for a suitable and simple extraction of physical properties induced by the PR effect consists of a combination between the variable stripe length (VSL) method<sup>[42]</sup> and the measurement of the frequency-modulated waveguided PL, as illustrated in Figure 2d (more technical details can be found in Section 2 of the Supporting Information). On the one hand, the VSL method consists of illuminating the surface of the waveguide with a laser spot focused on a  $800 \times 200 \mu\text{m}$  stripe, and allows the characterization of the signal losses by the dependence of the PL intensity as a function of the distance between the line and the waveguide edges ( $z$ ), as indicated in Figure 2d. On the other hand, the phase shift ( $\Delta\phi$ ) between the excitation and collected PL signal can be analyzed as a function of  $z$  (Figure 2e), as the basis to extract the effective PL decay time ( $\tau$ ) following the frequency modulation spectroscopy principles (see next section for the specific equations).<sup>[43]</sup> Figure 2f presents an illustrative characterization of the PL at  $z = 0$  (green curve) and  $z = 2.5 \text{ mm}$  (dark yellow curve). The PL spectrum at  $z = 0$  (green curve in Figure 2f) is very similar to that measured in the colloidal solution (green curve in Figure 2a), hence this PL spectrum is mainly determined by primary photons produced after the absorption of the laser pumping beam; accordingly, a decay time  $\tau \approx 3 \text{ ns}$  is deduced from  $\Delta\phi(\omega)$  (green symbols and fitting curve in Figure 2e) that agrees with the exciton recombination time reported for CsPbBr<sub>3</sub> PNCs at room temperature.<sup>[50]</sup> Besides, the waveguided PL spectrum measured at  $z = 2.5 \text{ mm}$  (dark yellow curve in Figure 2f) is clearly red-shifted and, accordingly, an effective PL time decay  $\tau \approx 7 \text{ ns}$  is deduced from  $\Delta\phi(\omega)$  (dark yellow symbols and fitting curve in Figure 2e). Both signatures are due to the reabsorption effect and the propagation of a secondary photon flux produced by several (re)absorption/(re)emission events.

### 3. Outcoupling of Recycled Photons at Long Distances: $\omega$ -Modulated PL

Figure 3a–c presents the PL spectra decoupled at the output edge of the waveguide as a function of  $z$ , using PNC films of different thicknesses:  $d_1 = 50, 100$  and  $200 \text{ nm}$ , in Figure 3a–c, respectively. The geometrical parameter  $d_1$  has an important impact on the outcoupled PL spectra because it dictates the confinement of the fundamental mode within the PNC region,  $\Gamma$ :

$$\Gamma = \frac{\int_{d_2}^{d_1+d_2} S(x) \cdot dx}{\int_{-\infty}^{\infty} S(x) \cdot dx} \quad (1)$$

where  $S(x)$  is the pointing vector of the fundamental optical mode of the waveguide, whose spatial dependence has been obtained with a transfer matrix algorithm by considering the refractive index of each layer. It is worth noting here that the limit values for  $\Gamma$  would mean:

- i.  $\Gamma$  tends to 0, indicates that incident laser beam is not producing at all a primary (nor secondary photon flux at the PNC emission wavelengths), i.e., the structure would be practically “transparent.”
- ii.  $\Gamma$  tends to 1, indicates that incident laser beam will be mostly absorbed at short  $z$  and primary (photons emitted subsequently) and secondary (photons produced after more than one absorption/emission process) photon fluxes are traveling exclusively along the PNC film (ideal waveguide).

For the three samples with different film thicknesses of CsPbBr<sub>3</sub> PNCs, the PL spectra at  $z = 0$  are similar to that measured in standard thin films (see for example ref. [39] in which we used nanocrystals similarly synthesized), indicating that the primary photons are dominant in the illuminated area, like in backscattering geometry for PL measurements. However, when a path for the primary photons is available without pumping ( $z > 0$ ) the outcoupled PL spectra experience a redshift caused by a non-negligible PR effect. For  $d_1 = 50 \text{ nm}$  (Figure 3a), waveguided PL spectra at different  $z$  exhibit a small redshift and, accordingly, a very weak PR effect, which is ascribed to the small  $\Gamma \approx 20\%$  of the total power distribution for this thin layer. Indeed, this case can be analogous to an incident light spot (normal incidence) much larger than the lateral dimensions of the sample. On the opposite,  $\Gamma$  increases up to  $\approx 80\%$  in the sample with  $d_1 = 200 \text{ nm}$  and, consequently, the PL spectra shift to longer wavelengths, see Figure 3b,c. In particular, for  $d_1 = 100\text{--}200 \text{ nm}$  the PL peak exhibits a monotonous redshift from  $523$  up to  $531 \text{ nm}$  for  $z = 2.5 \text{ mm}$  (brown and black symbols in Figure 3d), as compared to the practically constant value for  $d_1 = 50 \text{ nm}$  (red symbols in Figure 3d).

The redshift observed in these samples (Figure 3a–c) is correlated with the attenuation of the PL presented in Figure 3e. The PL intensity ( $I_{\text{PL}}$ ) measured as a function of  $z$  obeys the equation:<sup>[42]</sup>

$$I_{\text{PL}}(z) = A_1 \cdot e^{-z/L_{p1}} + A_2 \cdot e^{-z/L_{p2}} \quad (2)$$

where  $I_{\text{PL}}(0) = A_1 + A_2$  defines the PL intensity at  $z = 0$ , being  $A_i$  and  $L_{pi}$  the relative intensity and propagation length of the mode  $i$ . In this way,  $I_{\text{PL}}(z)$  follows two exponential decays that depend on emitted light losses at the PL peak wavelength. The first one is characterized by  $L_{p1} = 180 \pm 10, 100 \pm 20,$  and  $150 \pm 20 \mu\text{m}$  for  $d_1 = 50, 100,$  and  $200 \text{ nm}$ , respectively, and corresponds to the fundamental mode. The higher value of  $L_{p1}$  as compared to that deduced with the mode analysis ( $\approx 10 \mu\text{m}$ ) can be attributed here to a filling factor (ratio of space volume filled by PNCs over total volume) smaller than one in PNC films, and the fact that  $I_{\text{PL}}$  is integrated for the whole PL spectra. The second propagation length is about  $L_{p2} = 750 \pm 250 \mu\text{m}$  for all samples and represents about 20–25% ( $A_2/(A_0 + A_1)$ ) of the total PL intensity. We believe that this second propagation length can be directly related to the PR effect, i.e., associated with the secondary photon flux formed by the multiple (re)absorption and (re)emission processes that occur in the waveguide. In this way, the second propagation length  $L_{p2}$  could be understood as a gain-assisted mechanism (arrow in Figure 3e) for the self-absorption losses. That is, in the absence of PR, the propagation of emitted photons will be limited by  $L_{p1}$  (dashed line

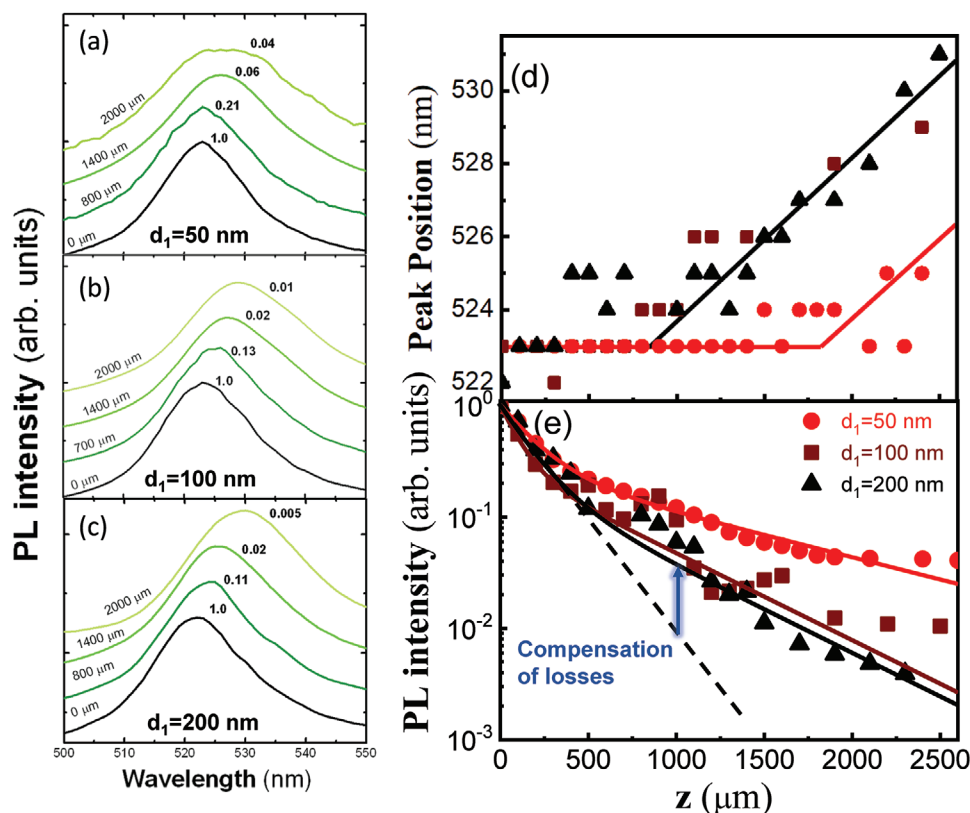


**Figure 3.** Waveguided PL spectra and outcoupled intensity. a–c) Normalized PL spectra collected for different waveguide lengths from  $z = 0$  to  $z = 2000 \mu\text{m}$  that integrate PNC films of thicknesses a)  $d_1 = 50 \text{ nm}$ , b)  $d_1 = 100 \text{ nm}$  and c)  $d_1 = 200 \text{ nm}$ , where numbers indicate the PL peak intensity referred to the value at  $z = 0$ . d,e) PL peak wavelength and PL intensity as a function of  $z$ , respectively. Red, brown, and black symbols refer to  $d_1 = 50 \text{ nm}$ ,  $d_1 = 100 \text{ nm}$ , and  $d_1 = 200 \text{ nm}$  PNC films. Solid lines in (e) represent the fitting of the data to a bi-exponential decay function.

indicated in Figure 3e), but PR results in a longer propagation length or an enhancement of the PL signal at a given propagation distance  $z$  (indicated by a blue arrow in Figure 3e), as will be discussed below and in the next section.

Since PR comes from a sequence of multiple absorption and emission events during establishing the light signal propagation in the waveguide, different physical mechanisms influence its efficiency and potential applications. For example, this process can be modified by the radiative lifetime, non-radiative channels, Auger recombination, carrier diffusion, optical path associated with the optical geometry, diffusion of photons, among other mechanisms.<sup>[18,26]</sup> In this way, a fast characterization technique able to separate most of the contributions would be needed to provide the required information to engineer photon recycling in each device. Here, we propose the application of frequency-domain fluorescence spectroscopy (FD-spectroscopy)<sup>[43]</sup> to study the photon recycling effect on waveguided PL signal, which is mainly spectral (PL peak redshift) and temporal (slowdown of the PL decay time). The analysis of the frequency-modulated PL will give us the latter information, in analogy to the impedance spectroscopy significantly used for the analysis of photogenerated carrier transport in solar cells.<sup>[51]</sup> In particular, the finite exciton lifetime in the sample under study would affect the intensity and phase of the PL signal under sufficiently high modulation frequencies through the following transfer function:<sup>[43]</sup>

$$m(\omega) = (1 + \omega^2 \tau^2)^{-1/2} \quad (3)$$

$$\phi(\omega) = \tan^{-1}(\omega\tau) = \cos^{-1}[(1 + \omega^2 \tau^2)^{-1/2}] \quad (4)$$

Here,  $m(\omega)$  is the absolute value of the PL normalized by the response of the laser,  $\phi(\omega)$  is the phase difference between the reference signal and the PL,  $\tau$  is the effective decay time, and  $\omega = 2\pi f$ , where  $f$  is the frequency of the modulation introduced to the excitation laser.

For a multiexponential decay time function, Equations (3) and (4) can be generalized to:

$$N(\omega) = \frac{\sum_k \alpha_k \cdot \omega \cdot \tau_k^2}{(1 + \omega^2 \cdot \tau_k^2)} / \sum_k \alpha_k \cdot \tau_k \quad (5)$$

$$D(\omega) = \frac{\sum_k \alpha_k \cdot \tau_k}{(1 + \omega^2 \cdot \tau_k^2)} / \sum_k \alpha_k \cdot \tau_k \quad (6)$$

where  $\alpha$  corresponds to the weight of the  $k$  decay ( $\tau_k$ ), and  $N(\omega)$  and  $D(\omega)$  corresponds to the real and imaginary part of the detected signal, respectively. In order to provide the highest accuracy in the measurements, each experimental point was obtained after five averages and the signal was always kept at

least one-fold higher than the noise. Furthermore, since our experimentally available  $\omega$ -range is restricted to 1–2 MHz, very short as compared to the case of the electrical modulation in the well-known impedance spectroscopy,  $m(\omega)$  is not very sensitive given that the exciton lifetime  $\tau \sim 1/\omega \approx 3 \times 10^{-9}$  s. For this reason, we have chosen  $\tan(\phi(\omega))$  in Equation (4) as the most sensitive magnitude to extract  $\tau$ . This is also because  $\phi(\omega)$  can be measured by the lock-in amplifier with accuracy as low as 0.01 radians.

Figure 4a–c shows representative measurements for waveguides defined by PNC films with thicknesses  $d_1 = 50, 100,$  and  $200$  nm. Green, dark green, and dark yellow symbols correspond to  $z = 0$  mm,  $z = 1$  mm, and  $z = 2$  mm, respectively. In all cases, the low dispersion of the experimental data allows a nice fitting with the low pass filter model given by Equations (5) and (6). The PL kinetics is not only influenced by the spontaneous recombination of excitons ( $\approx 3.5$  ns), but also from trapping/detrapping mechanisms that delay PL decay times of HP materials up to  $1 \mu\text{s}$ , as we proposed in previous works.<sup>[50,52,53]</sup> Here, we believe that each process (exciton and trapping/detrapping) can be observed at its specific frequency range. Above  $0.5$  MHz or so, experimental data follows a linear variation whose slope is consistent with an effective decay time  $\tau_1$  ( $\tau$  later) in the range  $3$  to  $9$  ns depending on the thickness of the active layer,  $d_1$ , and the propagation distance,  $z$ , as shown in Figure 4a–c. See Section 2 of the Supporting Information for the complete variation of the fitting parameters with  $z$  and the different samples changing  $d_1$ . The decay time measured at short  $z$ ,  $3$ – $3.5$  ns, agrees with the recombination time of excitons reported for  $\text{CsPbBr}_3$  PNCs under low power excitation conditions at room temperature ( $< 1 \mu\text{J cm}^{-2}$ ).<sup>[39]</sup> Furthermore, we need to introduce

a longer decay time  $\tau_2 = 1.25 \pm 0.50 \mu\text{s}$  to reproduce the variation of the phase with a smaller slope in the low-frequency range ( $30$ – $300$  kHz). This longer second time is ascribed here to the trapping/detrapping mechanism and remains constant for the whole range of the geometrical parameters,  $d_1$ , and  $z$ , studied here. The ratio of weights ( $\alpha_1/\alpha_2$ ) in Equations (5) and (6) lies in the range  $10^{-5}$  to  $10^{-4}$ , which means a small contribution of the second and long decay time, i.e., small slope of phase for frequencies below  $0.3$  MHz in Figure 4a–c.

The radiative recombination of excitons (or exciton lifetime  $\approx 3$ – $3.5$  ns) would be the dominant mechanism at short propagation distances ( $z$ ). As  $z$  increases, a delay time is introduced in waveguided PL due to the enhancement of the PR effect by the longer path for secondary (re)absorbed/(re)emitted photons. As it was earlier proposed for  $\text{CsPbBr}_3$  microwires,<sup>[21]</sup> MAPI crystals,<sup>[10]</sup> MAPI films,<sup>[18]</sup> PR becomes more and more effective for longer  $z$  as most of primary/pumping photons are absorbed in less than one micron. This effect is not only giving rise to the red-shift of the PL spectrum of the PNC film, but also to an increase of the “effective” PL decay time.<sup>[21,32]</sup> In the present work, for  $z < 100 \mu\text{m}$  we measure  $\tau = 3$ – $4$  ns for the three samples with different thicknesses of the active layer, which means that PR propagation distance is significantly longer than  $100 \mu\text{m}$ . In measurements of waveguided PL at longer optical paths ( $z > 100 \mu\text{m}$ ), more and more multiple (re)absorption and (re)emission cycles are taking place, which in turn will introduce an additional delay for outcoupled photons, coming from a “secondary photon flux”, as observed in Figure 4d. The proposed waveguide structure allows the propagation of the recycled photons at distances longer than  $1$  mm, which is much higher than the “photon propagation length”

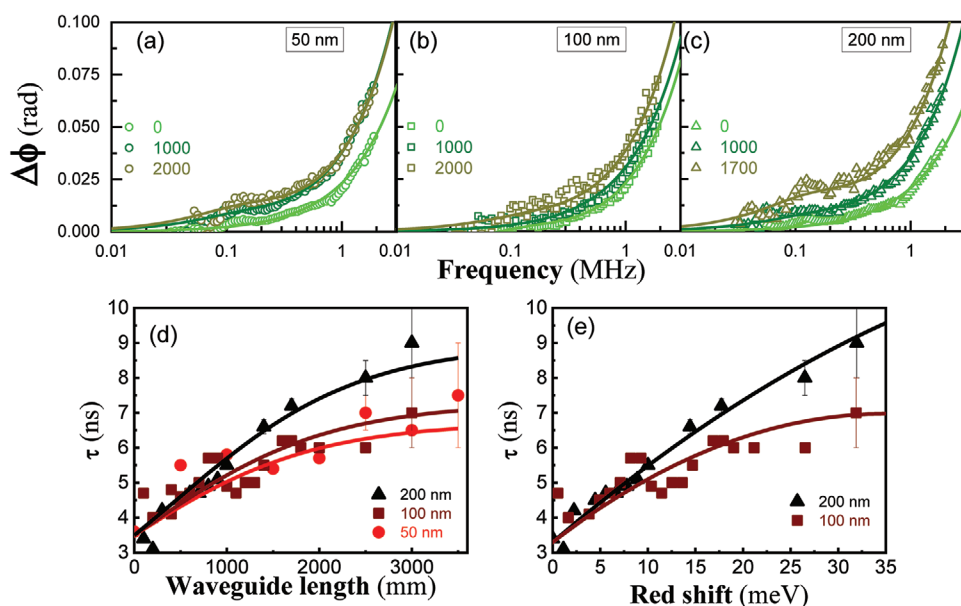


**Figure 4.** Measured phase and fitting to Equations (5) and (6) for extracting the effective decay time of waveguided PL.  $\tan(\phi(\omega))$  data for  $z = 0$  mm (green symbols),  $z = 1$  mm (dark green symbols) and  $z = 2$  mm (dark yellow symbols) for waveguides with: a)  $d_1 = 50$  nm, b)  $d_1 = 100$  nm, c)  $d_1 = 200$  nm. Solid lines show the data fitted through Equations (4) and (5). d) Decay times extracted in Figure 4a–c as a function of  $z$  for  $d_1 = 50$  nm (red symbols),  $d_1 = 100$  nm (brown symbols) and  $d_1 = 200$  nm (black symbols). The solid lines (with the same color code) correspond to the best fitting curves with the rate equation model defined by Equations (7) and (8). e) Correlation between the effective decay time and the Stokes shift for  $d_1 = 100$  nm (brown symbols),  $d_1 = 200$  nm (black symbols). Dotted lines correspond to a quadratic polynomial fitting representative of such strong correlation between both magnitudes.



estimated from other architectures (see Table S2, Supporting Information). Consequently, the present geometry introduces a certain increase of the decay time, from  $\tau \approx 3$  ns for  $z = 0$  mm to  $\tau \approx 9$  ns for  $z = 3$  mm, which results in a ratio  $(\tau/\tau_0) = 2$ , only reached with single crystals (see Table S2, Supporting Information).<sup>[41]</sup> Moreover,  $\tau$  increases (from 7 to 9 ns at  $z = 3$  mm) with the PNC thickness  $d_1$  (100 and 200 nm, respectively), because the TE<sub>0</sub> mode is more and more confined in the active layer ( $\Gamma = 80\%$  for  $d_1 = 200$  nm). We could take account of this phenomenology by the following rate equation system for the exciton and photon populations:

$$\frac{\partial n(z)}{\partial t} = \alpha \cdot \beta \cdot \gamma(z) - \frac{n(z)}{\tau_r} \quad (7)$$

$$\gamma(z) = I(0) \cdot \frac{1}{\alpha} \cdot (1 - e^{-\alpha z}) \quad (8)$$

where  $\beta$  is a parameter related to the reabsorption,  $I(0)$  the flux of primary photons at  $z = 0$ ,  $\gamma(z)$  the integration of the primary flux of photons at the position  $z$ , and  $\alpha$  the attenuation of the primary photons. Equation (7) is the rate equation of the exciton population ( $n(z)$ ),<sup>[39]</sup> where the term  $\alpha \cdot \beta \cdot \gamma$  represents an excitonic generation rate dependent on the primary PL photon flux. Equation (8) indicates the integrated population of primary photons at a distance  $z$ .<sup>[42]</sup> The experimental variation of the effective decay time with the propagation distance can be nicely fitted by means of Equations (7) and (8), see solid lines in Figure 4d, with the following parameters:  $\tau_r = 3.5$  ns,  $\alpha = 0.0005 \mu\text{m}^{-1}$ , and  $\beta = 0.06, 0.07$ , and  $0.1 \text{ J}^{-1} \text{ m}^{-1}$  for waveguides with  $d_1 = 50, 100$ , and  $200$  nm, respectively. The large value of  $\beta$  required to reproduce the experiments confirms the importance of the PR effect and indicates that PR can be interpreted as a photon gain mechanism in the waveguides. The increase of  $\beta$  with  $d_1$  can be ascribed to the increase of the electric field confinement in the waveguide.

Furthermore, the value of  $\tau$  is strongly correlated with the redshift of the corresponding PL spectra measured at the same propagation distance in the three waveguides, as shown in Figure 4e (data symbols and the square-polynomial fitting). However, this correlation is not straightforward and cannot be accounted for by means of the rate equation system (7 and 8). For including the light wavelength, it would be necessary to consider the  $\lambda$ -variation of the exciton population proportional to PL spectrum and the absorption coefficient, other than the possible and unknown variation of  $\beta$ . These drawbacks can be better solved using the 1D Monte Carlo modeling proposed in the next section.

#### 4. The Physics behind the PR Effect and Enhancement in the Waveguide Architecture

The results presented in the previous section clearly indicate the influence of the PR in the dynamics of the light propagation along the waveguide. In particular, the photons extracted at the output edge of the sample are influenced by the PR effect that results in a redshift of the spectra and an increase of the apparent PL decay time. We propose here to apply a 1D Monte Carlo ray-tracing technique<sup>[54]</sup> to simulate the photon

population with time and distance within the optical waveguide. This modeling will be the basis to understand the experimental results presented in Figures 3 and 4 and extract (semi) quantitative information of the PR effect, which is important for imaging and developing new architectures in future optoelectronic and photonic devices with increased efficiency due to the PR effect.

This 1D Monte Carlo model explains quite reasonably how is taking place the propagation of photons generated by exciton recombination (in the different absorption/emission cycles) inside the waveguide (see the qualitative illustrations in Figure 5a and the Video S1, Supporting Information, animation). For this purpose, the model analyses the temporal evolution of each photon injected in the waveguide following the next steps:

- i. A flux of a primary is spontaneously generated at the excitation stripe spot.
- ii. There is a probability of photon absorption by the PNCs embedded inside the structure as a function of the wavelength and the propagation distance ( $z$ ).
- iii. The absorbed photons generate a secondary flux of emitted photons whose propagation is, again, analyzed by the probability of absorption.

In fact, the simulated photon flux at distances above 2.5 mm yields a redshift in the order of 10 nm (see the 2D map in Figure 5b), in agreement with experimental data represented in Figure 3d. Moreover, the population of photons at each propagation distance indicates the influence of the PR by adding a delay that increases the effective PL decay time (over the value of the exciton recombination time),<sup>[21]</sup> as shown in Figure 5c. Clearly, the photon age increases with  $z$  and the most probable value for the photon population (dotted line in Figure 5c) explains the experimental values obtained for  $\tau$  in Figure 4d, as described in the previous section.

Under these conditions, the influence of the PR can be evaluated by calculating the number of reabsorption/reemission events (or PR events) along the waveguide. According to the map presented in Figure 5d, the photon propagation distance ( $z$ ) is linearly correlated with the number of PR events. For example, the number of PR events is around 35 per primary photon to travel a distance of 1 mm. In our experiments, the density of primary photons injected in the waveguide can be estimated as:

$$N = \alpha \cdot \frac{P \cdot \tau}{h \cdot \nu} \quad (9)$$

where  $\alpha$  is the absorption of the excitation beam at 450 nm (around  $1 \mu\text{m}^{-1}$ ),  $\tau$  the exciton recombination time without PR ( $\approx 3.5$  ns),  $P$  the excitation fluency ( $30 \text{ mW cm}^{-2}$ ) and  $h\nu$  the photon energy (2.375 eV). These numbers yield  $N = 2.75 \times 10^{12} \text{ photons cm}^{-3}$ , hence a total number of primary photons of  $8.8 \times 10^4$  injected in the excitation volume of around  $3.2 \times 10^{-8} \text{ cm}^3$  ( $800 \times 200 \times 0.2 \mu\text{m}^3$ ), which give rise to a total number of  $3.08 \times 10^6$  PR events along 1 mm of propagation distance. In particular, our 1D Monte Carlo model predicts that, under steady-state conditions, from  $N_0$  (total) injected photons (the algorithm imposes an injection of  $n_0$  photons per iteration—every  $\Delta t$ —until reaching the steady-state conditions,



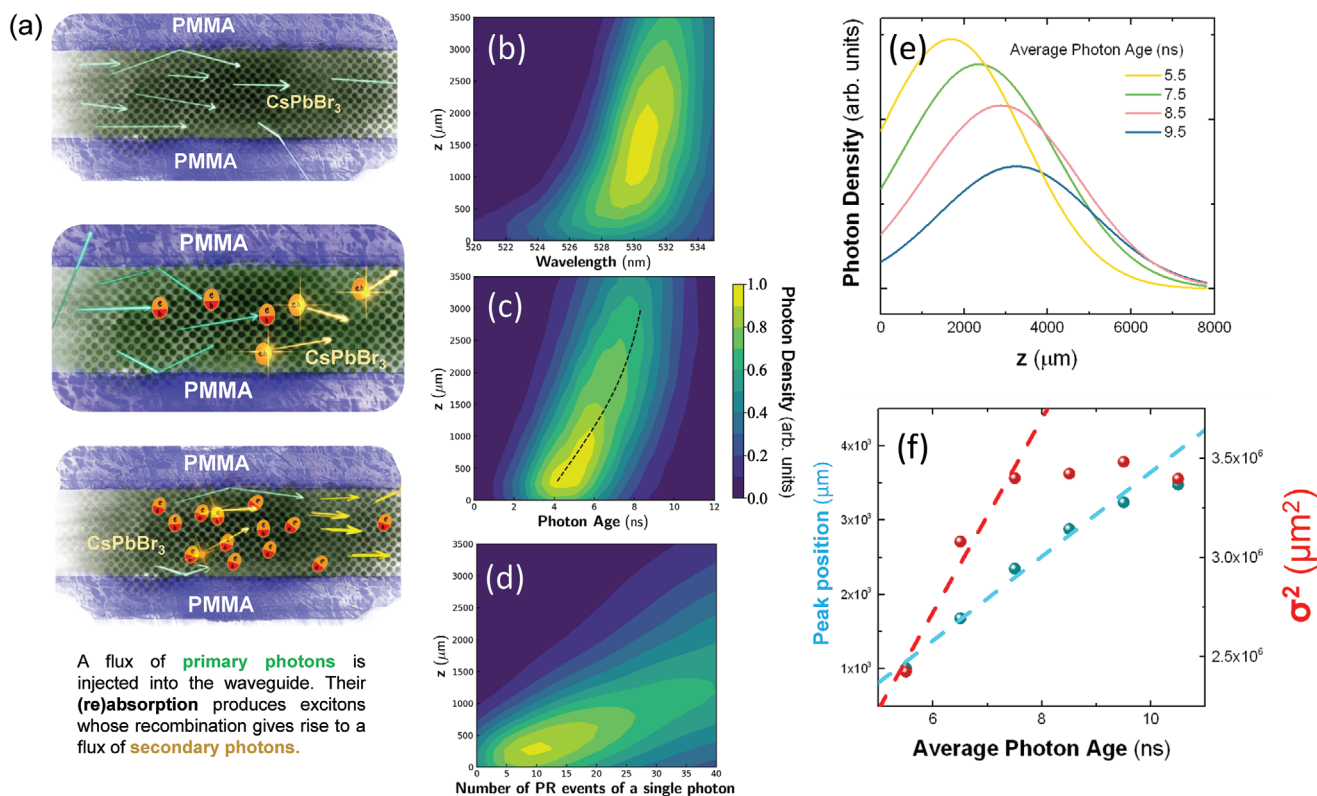


**Figure 5.** Simulation with a Monte Carlo algorithm. a) Illustration of the steps taken into account within the Monte Carlo algorithm: injected primary photons (top panel), generation of excitons (electron–hole pairs) and photons by exciton recombination (middle panel), (re)absorption–(re)emission processes giving rise to the secondary photon flux (bottom panel). b) Simulated map made from (time integrated) PL spectra as a function of the propagation distance. c) Spatial and temporal variation of the photon population (dotted line indicates the most probable value given by the photon population). d) Population of photons as a function of the propagation distance and the number of PR events. All 2D maps are normalized to the maximum photon density with the color scale indicated at the right of (c). e) Spatial distribution (Gaussian-like) of the photon population at different photon ages (averaged 1 ns around the indicated values, 5.5 to 9.5 ns). f) Peak position of the photon population (cyan symbols, right axis) and Gaussian variance  $\sigma^2$  as a function of the averaged photon age (red symbols, left axis). The variation of these magnitudes can be fitted (dashed lines in the plot) by a drift velocity of  $5.7 \times 10^5 \text{ m s}^{-1}$  and a diffusion coefficient  $D = 450 \text{ m}^2 \text{ s}^{-1}$ .

typically after  $>20\,000$  iterations, i.e.,  $N_0 = 20\,000n_0$ ) we get only  $5 \times 10^{-5} N_0$  of primary injected photons and  $0.01 N_0$  of secondary photons outcoupled at  $z = 3 \text{ mm}$ . That is, outcoupled secondary (recycled) photons are important at long propagation distances, being as high as 1% of injected photons in the waveguide, whereas the proportion of primary photons is negligible, only 0.005%, because they are mostly absorbed (as indicated in Figure 3e). This important claim would imply a significant increase of electron–hole pairs promoted to conduction–valence bands of the PNC film, which could be interpreted as a gain-assisted mechanism, in the sense of a propagation length enhancement, for the collected PL. The derived benefits in optoelectronic devices include an increase of the conversion efficiency in solar cells, with a major improvement of the photovoltage, or the enhancement of the outcoupling efficiency in light-emitting diodes.

Finally, the nature of the PR in the waveguide can be analyzed by studying the evolution of the secondary photon density ( $S$ ) with the propagation distance. Figure 5e presents the spatial distribution of the photon population at different photon ages (integrating over a window of 1 ns) as a function of  $z$ . Such spatial distribution for the different photon ages is represented by Gaussians (Figure 5e), as a result of the corresponding fitting applied to simulated data. The peak position of the Gaussians

increases with photon age, as also occurs for the variance (at least up to 8.5 ns). Therefore, the evolution of the secondary photon flux can be explained by Fick's law, where the drift term ( $v$ ) indicates the shift of the peak position with time (cyan circles in Figure 5f) and the diffusion term ( $D$ ) the broadening of the Gaussian variance (red circles in Figure 5f):

$$\frac{\partial S(z,t)}{\partial t} = D \frac{\partial^2 S(z,t)}{\partial z^2} - v \frac{\partial S(z,t)}{\partial z} \quad (10)$$

The concept of photon diffusion was introduced to model the multiple absorption/emission cycles as the scattering of the PL,<sup>[26]</sup> which would be dominant in the geometry of the thin film depicted in Figure 1a (see the simulation results in Figure S3, Supporting Information). In our sandwich waveguide geometry, the high confinement of the electromagnetic field in the active region (the film formed by PNCs) and the preferential direction derived from our excitation conditions results in a restricted influence of the diffusion term. Instead of this, the photons injected at  $z = 0$  are drifted due to a certain preferential propagation in the forward direction (in our 1D Monte Carlo model) imposed by the waveguide. At these conditions, the peak position shows a linear dependence with the photon age, see Figure 5f, with a slope of  $v \approx 5.7 \times 10^5 \text{ m s}^{-1}$

(cyan dashed line in Figure 5f) that corresponds to the “drift velocity” of photons along the propagation direction. With this velocity, one can estimate a transit (delay) time for recycled photons  $\tau_t \approx 5$  ns to travel 3 mm in the waveguide. If this time is added to the exciton recombination time, one obtains the measured effective decay time of near 9 ns. Since the secondary flux depends on the reabsorption efficiency and the exciton lifetime of emitted photons (here we take also into account the PL shape as in the above given illustration for question 2) inside the optical waveguide, we believe that these physical parameters and the geometrical and dielectric parameters of the structure (the thickness of the film, its dielectric constant and that of claddings determining the confinement factor in Equation 1), together with the size distribution of nanocrystals, are the main factors determining “drift velocity” and “diffusion coefficient” of photons in the perovskite nanocrystal structure studied here.

Simultaneously, a diffusion coefficient of around  $D \approx 450 \text{ m}^2 \text{ s}^{-1}$  is deduced from the variance of the spatial distribution of the photon population (red dashed line in Figure 5f). The diffusion term saturates because the drift is dominant in the proposed photonic architecture. Moreover, this  $D$  constant is consistent with the one obtained in the case of a standard thin film (Figure 1a),  $D = 420 \text{ m}^2 \text{ s}^{-1}$ , see Figure S3 (Supporting Information), where no directionality was imposed in our 1D Monte Carlo model. As expected, in the thin film case, only diffusive regime for the secondary photon flux is deduced from our simulation, i.e. represented by a linear increase of the Gaussian variance with time, as shown in Figure S3 (Supporting Information) (red dotted symbols and dashed fitting line). Furthermore, if diffusive regime dominated, as occurs for the thin film case, the time for traveling 3 mm would be 20 ns, four times longer than the value in the waveguide, considering that distance, 3 mm, as the diffusion length. It is also worth mentioning that our thin film made of PNCs does not hold carrier diffusion. This simplifies the modeling above, but it will be necessary to be considered in next future investigations involving the optimization of PR for photovoltaic devices.

## 5. Conclusions

In this work, PR mechanism is studied in thin films made of PNCs deposited by doctor blading and sandwiched by PMMA to define a waveguide structure on a Si/SiO<sub>2</sub> substrate. This configuration highly confines emitted light within the active PNC material by the TE<sub>0</sub> (TM<sub>0</sub>) propagation modes, hence it results optimum to enhance the PR effect with low losses along the propagation direction, for distances as long as several millimeters. Waveguided PL experiences a peak wavelength redshift with the propagation length in the order of 10 nm, which evidences the reabsorption effect. The impact of PR is corroborated by a correlation of such redshift with the effective decay time of outcoupled photons, as exciton recombination time and the delay introduced by the multiple absorption/emission events. For this purpose, a powerful characterization technique involving the VSL method and frequency-modulated spectroscopy was used to properly analyze the effective PL decay time.

We have shown that PR effect can be understood as a certain photon amplification mechanism, which properly formulated

(rate Equation 7) can account for the observed variation of the effective decay time with the propagation distance. The 1D Monte Carlo stochastic model developed in this work, where photon absorption/emission events can be naturally formulated in a probabilistic way, gives us more information in both space/time and wavelength domains. These simulations explain approximately the experimental results and predict recycled photons to propagate with low losses due to a certain directionality enhancement (“photon drift”) for photon propagation as compared to photon diffusion, which is the dominant behavior in the case of a standard thin film of a given thickness deposited on a certain substrate. From the comparison of our model to the real experimental results, we would conclude that the secondary photon flux, formed by recycled photons, propagates along the waveguide with a “drift velocity”  $v \approx 5.7 \times 10^5 \text{ m s}^{-1}$ , which is consistent with the observed increase of the effective decay time of outcoupled photons up to 9 ns ( $\approx 5.5$  ns over the exciton recombination time  $\approx 3.5$  ns) to travel along  $z = 3$  mm ( $\Delta t = v/z = 5.3$  ns). In the case of PR in a standard thin film, where no directionality would be defined for the emission events, photon diffusion is dominating, which would increase the average time necessary for the secondary photon flux to travel the same distance and, simultaneously, strongly reducing the outcoupled photon intensity at this distance. Consequently, the proposed photonic architecture enhances photogenerated carriers and it is expected to improve the PL signal and the photocurrent in future optoelectronic devices. Therefore, potential applications include photovoltaics and, more important, light emitting diodes, among other novel photonic concepts derived from the present work.

## Supporting Information

Supporting Information is available from the Wiley Online Library or from the author.

## Acknowledgements

Prof. Mehdi Ansari-Rad from the Shahrood University of Technology is acknowledged for his critical review of the present manuscript, suggestions and rich discussions. This project has received funding from the European Union’s Horizon 2020 research and innovation programme under grant agreement No 862656 (project DROP-IT) and European Research Council (ERC) via Consolidator Grant (724424, No-LIMIT), by the Spanish MINECO through projects no. TEC2017-86102-C2-1-R, PID2019-107348GB-I00, PID2019-107314RB-I00 and the national network of excellence PEROVSKITAS, and by Generalitat Valenciana (Spain) under projects PROMETEO/2018/098 and PROMETEO/2020/028. J.N.-A. also acknowledges the Spanish MINECO for his Ph.D. Grant No. BES-2015-074014.

## Conflict of Interest

The authors declare no conflict of interest.

## Data Availability Statement

The data that support the findings of this study are available from the corresponding author upon reasonable request.

## Keywords

CsPbBr<sub>3</sub>, frequency modulation spectroscopy, Monte-Carlo modeling, photon recycling, waveguides

Received: April 20, 2021

Revised: June 2, 2021

Published online:

- [1] W. P. Dumke, *Phys. Rev.* **1957**, *105*, 139.
- [2] Y. Xu, E. M. Tennyson, J. Kim, S. Barik, J. Murray, E. Waks, M. S. Leite, J. N. Munday, *Adv. Opt. Mater.* **2018**, *6*, 1701323.
- [3] S. Science, *Semicond. Sci. Technol.* **1993**, *8*, 1267.
- [4] M. A. Koc, S. N. Raja, L. A. Hanson, S. C. Nguyen, N. J. Borys, A. S. Powers, S. Wu, K. Takano, J. K. Swabeck, J. H. Olshansky, L. Lin, R. O. Ritchie, A. P. Alivisatos, *ACS Nano* **2017**, *11*, 2075.
- [5] S. D. Stranks, R. L. Z. Hoye, D. Di, R. H. Friend, F. Deschler, *Adv. Mater.* **2018**, *31*, 1803336.
- [6] Z. Gan, X. Wen, W. Chen, C. Zhou, S. Yang, G. Cao, K. P. Ghiggino, H. Zhang, B. Jia, *Adv. Energy Mater.* **2019**, *9*, 1900185.
- [7] S. De Wolf, J. Holovsky, S. J. Moon, P. Löper, B. Niesen, M. Ledinsky, F. J. Haug, J. H. Yum, C. Ballif, *J. Phys. Chem. Lett.* **2014**, *5*, 1035.
- [8] J. Maes, L. Balcaen, E. Drijvers, Q. Zhao, J. De Roo, A. Vantomme, F. Vanhaecke, P. Geiregat, Z. Hens, *J. Phys. Chem. Lett.* **2018**, *9*, 3093.
- [9] Z. Gan, W. Chen, L. Yuan, G. Cao, C. Zhou, S. Huang, X. Wen, B. Jia, *Appl. Phys. Lett.* **2019**, *114*, 011906.
- [10] H. Diab, C. Arnold, F. Lédée, G. Trippé-Allard, G. Delpont, C. Vilar, F. Bretenaker, J. Barjon, J. S. Lauret, E. Deleporte, D. Garrot, *J. Phys. Chem. Lett.* **2017**, *8*, 2977.
- [11] G. Xing, N. Mathews, S. S. Lim, N. Yantara, X. Liu, D. Sabba, M. Grätzel, S. Mhaisalkar, T. C. Sum, *Nat. Mater.* **2014**, *13*, 476.
- [12] L. Protesescu, S. Yakunin, M. I. Bodnarchuk, F. Krieg, R. Caputo, C. H. Hendon, R. X. Yang, A. Walsh, M. V. Kovalenko, *Nano Lett.* **2015**, *15*, 3692.
- [13] T. Kirchartz, F. Staub, U. Rau, *ACS Energy Lett.* **2016**, *1*, 731.
- [14] Z. Yang, Z. Yang, W. Yang, X. Yang, J. C. Greer, J. Sheng, B. Yan, J. Ye, *Energy Environ. Sci.* **2020**, *13*, 1753.
- [15] A. R. Bowman, M. Anaya, N. C. Greenham, S. D. Stranks, *Phys. Rev. Lett.* **2020**, *125*, 67401.
- [16] C. Cho, B. Zhao, G. D. Tainter, J. Lee, D. Di, F. Deschler, N. C. Greenham, R. H. Friend, *Nat. Commun.* **2020**, *11*, 1.
- [17] S. G. Motti, T. Crothers, R. Yang, Y. Cao, R. Li, M. B. Johnston, J. Wang, L. M. Herz, *Nano Lett.* **2019**, *19*, 3953.
- [18] L. M. Pazós-Outón, M. Szumilo, R. Lamboll, J. M. Ritcher, M. Crespo-Quesada, B. Ehrler, L. M. Pazos-Outon, M. Abdi-Jalebi, H. J. Beeson, M. Vruciniec, M. Alsari, H. J. Snaith, B. Ehrler, R. H. Friend, F. Deschler, *Science* **2016**, *351*, 1430.
- [19] Y. Fang, H. Wei, Q. Dong, J. Huang, *Nat. Commun.* **2017**, *8*, 14417.
- [20] T. Yamada, T. Aharen, Y. Kanemitsu, *Phys. Rev. Lett.* **2018**, *120*, 57404.
- [21] I. Dursun, Y. Zheng, T. Guo, M. De Bastiani, B. Turedi, L. Sinatra, M. A. Haque, B. Sun, A. A. Zhumekenov, M. I. Saidaminov, F. P. García De Arquer, E. H. Sargent, T. Wu, Y. N. Gartstein, O. M. Bakr, O. F. Mohammed, A. V. Malko, *ACS Energy Lett.* **2018**, *3*, 1492.
- [22] Y. Wang, X. Sun, R. Shivanna, Y. Yang, Z. Chen, Y. Guo, G. C. Wang, E. Wertz, F. Deschler, Z. Cai, H. Zhou, T. M. Lu, J. Shi, *Nano Lett.* **2016**, *16*, 7974.
- [23] E. Oksenberg, C. Fai, I. G. Scheblykin, E. Joselevich, E. L. Unger, T. Unold, C. Hages, A. Merdasa, *Adv. Funct. Mater.* **2021**, *31*, 2010704.
- [24] A. Sridharan, N. K. Noel, B. P. Rand, S. Kéna-Cohen, *J. Phys. Chem. C* **2021**, *125*, 2240.
- [25] D. Giovanni, M. Righetto, Q. Zhang, J. W. M. Lim, S. Ramesh, T. C. Sum, *Light: Sci. Appl.* **2021**, *10*, 2.
- [26] M. Ansari-Rad, J. Bisquert, *Phys. Rev. Appl.* **2018**, *10*, 034062.
- [27] M. G. Abebe, A. Abass, G. Gomard, L. Zschiedrich, U. Lemmer, B. S. Richards, C. Rockstuhl, U. W. Paetzold, *Phys. Rev. B* **2018**, *98*, 075141.
- [28] R. Brenes, M. Laitz, J. Jean, D. W. DeQuilletes, V. Bulovic, *Phys. Rev. Appl.* **2019**, *12*, 014017.
- [29] C. Cho, N. C. Greenham, *Adv. Sci.* **2021**, *8*, 2003559.
- [30] A. Bercegol, D. Ory, D. Suchet, S. Cacovich, O. Fournier, J. Rousset, L. Lombez, *Nat. Commun.* **2019**, *10*, 1586.
- [31] M. Saliba, W. Zhang, V. M. Burlakov, S. D. Stranks, Y. Sun, J. M. Ball, M. B. Johnston, A. Goriely, U. Wiesner, H. J. Snaith, *Adv. Funct. Mater.* **2015**, *25*, 5038.
- [32] F. Staub, T. Kirchartz, K. Bittkau, U. Rau, *J. Phys. Chem. Lett.* **2017**, *8*, 5084.
- [33] J. M. Richter, M. Abdi-Jalebi, A. Sadhanala, M. Tabachnyk, J. P. H. Rivett, L. M. Pazos-Outón, K. C. Gödel, M. Price, F. Deschler, R. H. Friend, *Nat. Commun.* **2016**, *7*, 13941.
- [34] I. Suárez, A. Larrue, P. J. Rodríguez-Cantó, G. Almuneau, R. Abargues, V. S. Chirvony, J. P. Martínez-Pastor, *Opt. Lett.* **2014**, *39*, 4962.
- [35] M. Signoretto, N. Zink-Lorre, I. Suarez, E. Font-Sanchis, Á. Sastre-Santos, V. S. Chirvony, F. Fernandez-La zaro, J. P. Martínez-Pastor, *ACS Photonics* **2017**, *4*, 114.
- [36] X. Zhang, C. Sun, Y. Zhang, H. Wu, C. Ji, Y. Chuai, P. Wang, S. Wen, C. Zhang, W. W. Yu, *J. Phys. Chem. Lett.* **2016**, *7*, 4602.
- [37] S. Yakunin, L. Protesescu, F. Krieg, M. I. Bodnarchuk, G. Nedelcu, M. Humer, G. De Luca, M. Fiebig, W. Heiss, M. V. Kovalenko, *Nat. Commun.* **2015**, *6*, 8056.
- [38] Y. Wang, X. Li, J. Song, L. Xiao, H. Zeng, H. Sun, *Adv. Mater.* **2015**, *27*, 7101.
- [39] J. Navarro-Arenas, I. Suárez, V. S. Chirvony, A. Gualdrón-Reyes, I. Mora-Seró, J. P. Martínez-Pastor, *J. Phys. Chem. Lett.* **2019**, *10*, 6389.
- [40] Q. A. Akkerman, M. Gandini, F. Di Stasio, P. Rastogi, F. Palazon, G. Bertoni, J. M. Ball, M. Prato, A. Petrozza, L. Manna, *Nat. Energy* **2017**, *2*, 16194.
- [41] T. Yamada, Y. Yamada, Y. Nakaike, A. Wakamiya, Y. Kanemitsu, *Phys. Rev. Appl.* **2017**, *7*, 014001.
- [42] H. Gordillo, I. Suarez, R. Abargues, P. Rodriguez-Canto, J. P. Martinez-Pastor, *IEEE Photonics J.* **2013**, *5*, 2201412.
- [43] J. R. Lakowicz, *Principles of Fluorescence Spectroscopy*, Springer, New York **2006**.
- [44] M. Ansari-Rad, J. Bisquert, *J. Phys. Chem. Lett.* **2017**, *8*, 3673.
- [45] G. Lifante, *Integrated Photonics: Fundamentals*, Wiley, New York **2002**.
- [46] H. Benisty, R. Stanley, M. Mayer, *J. Opt. Soc. Am. A* **1998**, *15*, 1192.
- [47] M. Zhao, Y. Shi, J. Dai, J. Lian, *J. Mater. Chem. C* **2018**, *6*, 10450.
- [48] E. Palik, *Handbook of Optical Constants of Solids*, Elsevier, Oxford 1998
- [49] Q. Shang, C. Li, S. Zhang, Y. Liang, Z. Liu, X. Liu, Q. Zhang, *Nano Lett.* **2020**, *20*, 1023.
- [50] V. S. Chirvony, S. González-Carrero, I. Suárez, R. E. Galian, M. Sessolo, H. J. Bolink, J. P. Martínez-Pastor, J. Pérez-Prieto, *J. Phys. Chem. C* **2017**, *121*, 13381.
- [51] S. M. Yoo, S. J. Yoon, J. A. Anta, H. J. Lee, P. P. Boix, I. Mora-Seró, *Joule* **2019**, *3*, 2535.
- [52] V. S. Chirvony, K. S. Sekerbayev, H. Pashaei Adl, I. Suárez, Y. T. Taurbayev, A. F. Gualdrón-Reyes, I. Mora-Seró, J. P. Martínez-Pastor, *J. Lumin.* **2020**, *221*, 117092.
- [53] V. S. Chirvony, J. P. Martínez-Pastor, *J. Phys. Chem. Lett.* **2018**, *9*, 4955.
- [54] K. Gopalsamy, B. D. Aggarwala, *ZAMM - J. Appl. Math. Mech./Z. Angew. Math. Mech.* **1970**, *50*, 759.